

Querying Autonomous Vehicle Point Clouds: Enhanced by 3D Object Counting with CounterNet

Xiaoyu Zhang
RMIT University
Melbourne, Australia
xiaoyu.zhang5@student.rmit.edu.au

Zhifeng Bao*
Queensland University
Brisban, Australia
zhifeng.bao@uq.edu.au

Hai Dong†
RMIT University
Melbourne, Australia
hai.dong@rmit.edu.au

Ziwei Wang
CSIRO
Brisbane, Australia
ziwei.wang@data61.csiro.au

Jiajun Liu
CSIRO
Brisban, Australia
jiajun.liu@csiro.au

Abstract

Autonomous vehicles generate massive volumes of point cloud data, yet only a subset is relevant for specific tasks such as collision detection, traffic analysis, or congestion monitoring. Effectively querying this data is essential to enable targeted analytics. In this work, we formalize point cloud querying by defining three core query types: RETRIEVAL, COUNT, and AGGREGATION, each aligned with distinct analytical scenarios. All these queries rely heavily on accurate object counts to produce meaningful results, making precise object counting a critical component of query execution. Prior work has focused on indexing techniques for 2D video data, assuming detection models provide accurate counting information. However, when applied to 3D point cloud data, state-of-the-art detection models often fail to generate reliable object counts, leading to substantial errors in query results. To address this limitation, we propose CounterNet, a heatmap-based network designed for accurate object counting in large-scale point cloud data. Rather than focusing on accurate object localization, CounterNet detects object presence by finding object centers to improve counting accuracy. We further enhance its performance with a feature map partitioning strategy using overlapping regions, enabling better handling of both small and large objects in complex traffic scenes. To adapt to varying frame characteristics, we introduce a per-frame dynamic model selection strategy that selects the most effective configuration for each input. Evaluations on three real-world autonomous vehicle datasets show that CounterNet improves counting accuracy by 5% to 20% across object categories, resulting in more reliable query outcomes across all supported query types.

*The work was done while Zhifeng Bao was at RMIT University.

†Hai Dong is the corresponding author.

Permission to make digital or hard copies of all or part of this work for personal or classroom use is granted without fee provided that copies are not made or distributed for profit or commercial advantage and that copies bear this notice and the full citation on the first page. Copyrights for components of this work owned by others than the author(s) must be honored. Abstracting with credit is permitted. To copy otherwise, or republish, to post on servers or to redistribute to lists, requires prior specific permission and/or a fee. Request permissions from permissions@acm.org.

Conference acronym 'XX, Woodstock, NY

© 2018 Copyright held by the owner/author(s). Publication rights licensed to ACM.

ACM ISBN 978-1-4503-XXXX-X/2018/06

<https://doi.org/XXXXXXX.XXXXXXX>

CCS Concepts

• Computing methodologies → Computer vision problems.

Keywords

Point cloud, retrieval, query, autonomous vehicle

ACM Reference Format:

Xiaoyu Zhang, Zhifeng Bao, Hai Dong, Ziwei Wang, and Jiajun Liu. 2018. Querying Autonomous Vehicle Point Clouds: Enhanced by 3D Object Counting with CounterNet. In *Proceedings of Make sure to enter the correct conference title from your rights confirmation email (Conference acronym 'XX)*. ACM, New York, NY, USA, 15 pages. <https://doi.org/XXXXXXX.XXXXXXX>

1 Introduction

The rise of autonomous driving has significantly increased the importance of point cloud data analysis, as autonomous vehicles heavily rely on point clouds to perceive their surroundings accurately. While vast amounts of data are collected—3D detection alone can generate approximately 5TB of point cloud data per hour [23]—not all data is relevant to every training task. For instance, detecting vehicle collisions and analyzing traffic congestion differ in their focus. Collision detection often involves identifying sudden, localized changes in vehicle count within short time frames, while congestion analysis requires aggregating vehicle counts over longer durations to identify sustained traffic buildup. These tasks, therefore, depend on different object types, time scales, and aggregation strategies, reinforcing the need for flexible point cloud analytics designed for specific use cases.

To support this, we define a query model that captures common patterns of analytical interest. Drawing on prior work in traffic video and point cloud querying, we identify three key query types: RETRIEVAL [20, 21, 30], COUNT [6], and AGGREGATION [3]. These cover a broad range of analysis needs for point cloud data, as illustrated in Figure 1. Specifically, RETRIEVAL queries extract frames that satisfy specific conditions, useful for tasks such as object tracking and scene filtering. COUNT queries quickly quantify how many frames meet a given condition, enabling statistical analysis, monitoring, and quality control. AGGREGATION queries summarize patterns across multiple frames, supporting trend analysis.

These query types form the foundation of our approach. However, their effectiveness relies heavily on accurate object counts

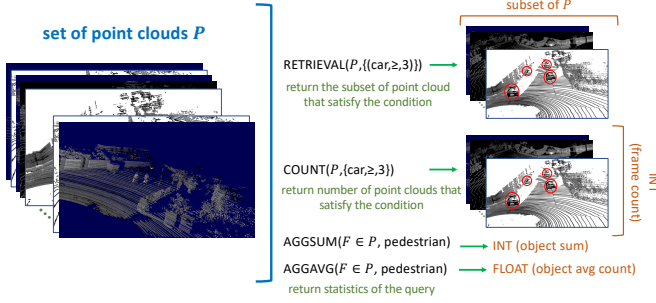


Figure 1: Example of different query types

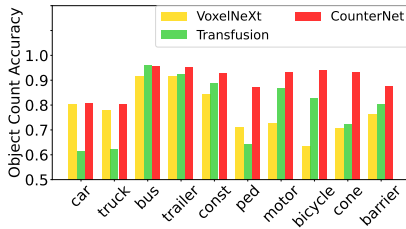


Figure 2: Counting ACC of baselines v.s. CounterNet (ours)

within individual frames. Unfortunately, current 3D detection models struggle to provide reliable counts across object categories, as we show in Figure 2. This undermines the assumption made by many existing query systems that detection outputs can serve as ground truth.

Prior work mostly focused on 2D traffic video querying [3, 6, 20, 21]. These studies generally assume that 2D object detection provides ground truth semantic information, and focus primarily on building efficient and effective indexing mechanisms to reduce the cost of query execution. For example, Blazelt [20] and TASTI [21] use proxy models to filter simple scenes, Seiden [3] uses sampling to minimize model invocations, and Figo [6] dynamically selects detectors based on video complexity. Although fewer works address 3D point cloud querying, approaches like MAST [30] extend Seiden [3] to the 3D domain by incorporating the spatial-temporal filters into the indexing process. These methods inherit a key assumption from their 2D counterparts: that object detection models yield ground truth results to serve as a foundation for query execution.

However, this assumption does not hold in the 3D point cloud setting. As shown in Figure 2, SOTA 3D detection models such as VoxelNext [9] and TransFusion [2] exhibit significant variance in object counting accuracy across different classes of objects. As a result, existing 3D query systems, which rely on indexing over potentially inaccurate outputs, struggle to deliver trustworthy results. Unlike these indexing-focused approaches, our work takes a different path: we focus on improving object counting accuracy in point cloud data, a foundational requirement for reliable query execution. Notably, rather than improving indexing itself, we target a more fundamental problem that current methods tend to overlook.

We propose CounterNet, a heatmap-based baseline designed for accurate object counting in complex traffic scenes. Our approach focuses on enhancing semantic information extraction from point cloud frames, with a particular emphasis on achieving precise, category-aware object counts. To improve its adaptability across object types and sizes, we refine CounterNet to support multi-class counting through scale-aware mechanisms. In addition, we introduce a per-frame dynamic model selection strategy, which assigns the most suitable counting model configuration to each frame based on its complexity, further boosting overall query accuracy without sacrificing efficiency. It is worth noting that our study’s primary focus is the query accuracy rather than efficiency.

Our contributions are summarised as below:

- To support query accuracy, we introduce CounterNet, a heatmap-based network that serves as our baseline solution. CounterNet focuses on detecting object centers, enabling accurate and efficient object counting within large-scale traffic point cloud frames (Section 4).
- We enhance CounterNet with a feature map partitioning strategy to improve performance in dense object counting (Section 5.1). To better handle large objects, we introduce overlapping partitions, providing a lightweight and effective solution (Section 5.2). Finally, we propose per-frame dynamic model selection, which adaptively selects the most suitable model trained with different partition numbers and overlap ratios for each frame (Section 5.3).
- We evaluated our approach on three autonomous vehicle datasets across three query types. The results show that CounterNet significantly outperforms 3D object detection models in query accuracy. Adding partitioning to CounterNet notably improved the detection of small objects, particularly in high-density scenes. Introducing overlaps between partitions further boosted performance across all object categories (Section 6).

2 Related Work

Video Data Querying and Indexing. Most of the related studies have focused on video data querying. Benefiting from advances in object detection in images, such as ResNet [15], Mask R-CNN [14], and YOLO [19], recent studies on video querying has primarily focused on indexing techniques to enhance query efficiency. For example, studies [6, 20, 21] utilise proxy models for fast indexing. To be specific, Kang et al. [20] introduced a specialized neural network as a similarity model, employing a compact ResNet architecture. Kang et al. [21] proposed a low-cost embedding deep neural network (DNN) that was trained using triplet loss. Cao et al. [6] focused on the ensemble of various models applied to different video segments, with the primary task being the strategic segmentation of video frames and matching segments with appropriate query models. In the most recent work, SEIDEN [3] constructed the index by effectively sampling the most important frames, allowing only these selected frames to be processed by the detection model for semantic information extraction, considering the high cost of running detection models. Additionally, SEIDEN leveraged object information extracted by the detection model to linearly predict the contents of non-sampled frames, enabling full indexing.

While these video-based techniques have demonstrated strong performance in their domain, their assumptions and design choices

limit their applicability to 3D point cloud data. Specifically, point cloud data presents two challenges that are neglected in these studies: (1) Point cloud data is considerably more complex than image data [38], making it difficult to achieve effective information extraction with proxy models with simple regression. (2) Detection models for point clouds do not perform as well as those for images, meaning that even with a detection model, there is no guarantee of query accuracy in point clouds.

Point Cloud Data Querying and Indexing. Building on SEIDEN’s framework, Li et al. [30] extends this approach to traffic point cloud data. It further enhances sampling by incorporating reinforcement learning with a spatially informed reward function and predicts the contents of non-sampled frames using spatial-temporal information extracted from sampled frames via the detection model. Similar to video query solutions, these studies primarily focus on improving query efficiency through optimized indexing. However, they often overlook the detection model’s actual performance in extracting semantic information from point cloud frames.

3D Object Detection in Point Clouds. 3D object detection employs a backbone for feature extraction and a detection head for task-specific outputs. Early works such as PointNet [38], PointNet++ [39], and VoxelNet [52] laid the foundation for 3D feature extraction. Later advancements [24, 33, 50] introduced improved feature extraction methods. Detection heads in 3D systems follow two primary approaches: anchor-based [8, 25, 40, 47, 48] and center-based [2, 9, 43, 51].

Despite substantial progress, these detection models are not designed for querying tasks. Detection focuses on object identification, whereas querying emphasizes extracting task-specific information, requiring tailored solutions.

Object Counting in Images and Point Cloud. The object count within video frames is crucial for supporting queries. Numerous studies have addressed object counting [7, 10, 26, 41, 46], noting that counting becomes significantly harder as the number of objects increases. Recent research has utilized textual information to improve accuracy [18, 22]. However, 3D data presents greater challenges than 2D due to the irregular distribution of points in point cloud frames, unlike the fixed grids of 2D images.

While some studies have investigated 3D object counting [17, 29, 36], they often focus on simpler scenarios like pedestrian or crop counting. These methods struggle with the complexity of autonomous vehicle scenes, which feature diverse object types in a single frame.

3 Problem Definition

Autonomous vehicles generate extensive point cloud data, which is crucial for navigation and environmental understanding. Since onboard systems prioritize real-time processing, they usually have limited storage. Instead, point cloud data is transmitted to a remote, e.g., edge server, enabling centralized processing and analysis [32, 35, 44]. Following Liu et al. [32], the data collected by the vehicle is uploaded to the cloud, and a NoSQL database is used to store the extracted features for querying. To achieve this, we first define the query types.

Preliminary. We denote \mathcal{P} as a set of point cloud frames, where each point cloud frame $p \in \mathcal{P}$ is a vector in \mathbb{R}^3 , representing the coordinates of a point in three-dimensional space.

Query Types. We define the three query types: RETRIEVAL, COUNT, and AGGREGATION. Figure 1 demonstrates an example of each query before our formal definitions.

DEFINITION 1 (RETRIEVAL QUERY). *The RETRIEVAL Query extracts point cloud frames from \mathcal{P} where multiple objects q_1, q_2, \dots, q_n appear based on specific count constraints ct_1, ct_2, \dots, ct_n . Each object has a comparison operator $op \in (\leq, \geq, =)$ to specify how its count is evaluated.*

$$\text{RETRIEVAL}(\mathcal{P}, \{(q_1, op, ct_1), (q_2, op, ct_2), \dots, (q_n, op, ct_n)\}) \\ = \{p \in \mathcal{P} \mid \forall i, \sum_{o \in p.objs} \mathbb{I}(o = q_i) op ct_i\}$$

where $\mathbb{I}(\cdot)$ is an indicator function that evaluates to 1 if the condition is true, and 0 otherwise.

DEFINITION 2 (COUNT QUERY). *The COUNT Query returns the number of frames in \mathcal{P} where a specified object q appears, satisfying the count condition (op, ct) :*

$$\text{COUNT}(\mathcal{P}, q, op, ct) = |\{p \in \mathcal{P} \mid \sum_{o \in p.objs} \mathbb{I}(o = q) op ct\}|$$

DEFINITION 3 (AGGREGATION QUERY). *The AGGREGATION Query provides statistical insights over \mathcal{P} for a specified object q . We define two aggregation functions: sum and average.*

$$\text{AGGSUM}(\mathcal{P}, q) = \sum_{p \in \mathcal{P}} \sum_{o \in p.objs} \mathbb{I}(o = q) \\ \text{AGGAVG}(\mathcal{P}, q) = \frac{1}{|\mathcal{P}|} \sum_{p \in \mathcal{P}} \sum_{o \in p.objs} \mathbb{I}(o = q)$$

4 Method: CounterNet

Data Model. Given that object count is the most important information for querying [3, 6, 20, 21], to accommodate the distributed nature of point cloud data collected by autonomous vehicles, instead of directly following the SQL-like relational database [11, 28, 34], we define a NoSQL data model as the document-like structure. The detailed definition can be found in Appendix C.1.

Design Motivation of CounterNet. The most straightforward method for obtaining object counts is through a regression model. However, a single point cloud frame contains vast amounts of information, including multiple objects in varying numbers, making it difficult for a regression model to capture such fine-grained details. Alternatively, object detection models are commonly used for counting, but they focus heavily on localizing objects, such as drawing accurate bounding boxes and determining object orientation. This complexity causes them to underperform in tasks focused solely on object counting.

It motivated us to develop a new method, which has the following properties: (1) To mitigate the limitation in the regression model, the method should be capable of detecting the appearance of the object in the region of the point cloud for a more fine-grained detection. (2) To mitigate the limitation brought by the detection model, the method should concentrate on detecting the appearance of object instead of spending efforts on the localization of objects. **Network Architecture.** We propose to utilise heatmaps for object counting, as illustrated in Figure 3. The objective of this approach is to detect object centers, which are represented as peaks in the heatmap. This method satisfied the two expected property mentioned above: (1) Compared to simple regression, the heatmap emphasizes identifying object appearances by detecting centers, resulting in more accurate counts. (2) It simplifies the detection task

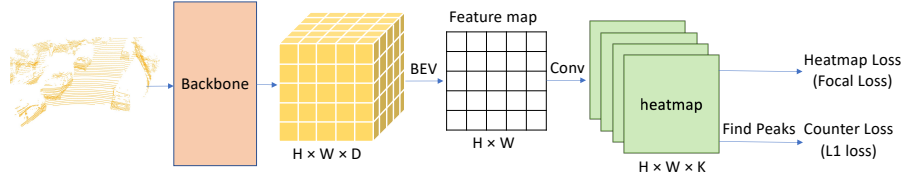


Figure 3: CounterNet Architecture. Given a point cloud frame, the features extracted from the backbone (e.g., VoxelNet) are projected onto a 2D feature map with a bird's eye view (BEV) projection via z-axis. Subsequently, a heatmap is generated for each of the K object categories based on the feature map. We use focal loss to ensure effective heatmap generation. We identify peaks within the heatmaps to get counter loss, which supervises the network to predict accurate object counts.

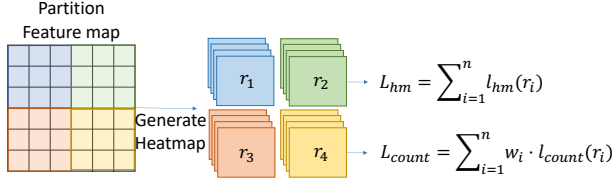


Figure 4: Feature Map Partition

by disregarding object size and orientation, focusing exclusively on detecting the object centers to identify their presence.

Heatmap. With the projected feature map, we generate a K -channel heatmap ($K = |C|$), where each channel corresponds to a specific object class. To train the heatmap, we utilise the ground truth positions of objects, annotating object centers with higher values and surrounding areas with lower values, which we utilise the Gaussian Kernel for a smooth [27, 49, 51].

Object Counting via Threshold-based Peak Detection. We count objects by finding local peaks in the heatmap. Those peaks are detected object centers. Specifically, we apply a 2D local maxima algorithm¹ to identify object centers, which then allows us to estimate both the count and approximate positions of the objects. Thresholding is crucial for reducing noise. To suppress noise in low-activation regions of heatmaps, we apply a fixed threshold to the predicted heatmap before applying local maxima detection. This ensures that only confident peaks, corresponding to likely object centers, are retained. The threshold is defined during the training stage. Since the heatmap values are normalized within the range of 0 to 1, we select a mid-range value as the threshold to ensure effective filtering (i.e., 0.5). Intuitively, the model is expected to assign higher values (above 0.5) to regions corresponding to object grids, while non-object regions will have lower values (below 0.5). **Loss.** As shown in Figure 3, we use two losses, focal loss and counter loss, to supervise the network for accurate counting.

We use the focal loss [31] to supervise the generation of the heatmap, as defined in Equation 1. In this equation, \hat{Y}_{xy} represents the predicted probability at location (x, y) in the heatmap, while Y_{xyc} denotes the ground truth label for object c , with $Y_{xyc} = 1$ indicating the presence of an object center. The term N refers to the number of positive samples (i.e., locations where $Y_{xyc} = 1$), which is used to normalize the loss. The parameter α is a focusing factor.

We take the value $\alpha = 2$ by following [51].

$$L_{hm} = \frac{-1}{N} \sum_{\hat{y}} \begin{cases} (1 - \hat{Y}_{xyc})^\alpha \log(\hat{Y}_{xyc}) & \text{if } Y_{xyc} = 1 \\ (1 - Y_{xyc})^\alpha \log(1 - \hat{Y}_{xyc}) & \text{otherwise} \end{cases} \quad (1)$$

We use thresholded local maxima on the heatmap to derive the object count. To supervise this process, we introduce an L1 loss for counting accuracy as shown in Equation 2. In this equation, y represents the predicted count, while \hat{y} represents the ground truth count. The count loss provides an additional supervisory signal to the heatmap, ensuring that regions corresponding to object centers exceed the threshold while other regions remain below it. Additionally, while the focal loss provides direct supervision for the heatmap, the count loss serves as auxiliary supervision for the entire network, guiding it toward more precise object counting results.

$$L_{count} = \frac{1}{|C|} \frac{1}{|\mathcal{P}|} \sum_{j=1}^{|C|} \sum_{i=1}^{|\mathcal{P}|} |y_{ji} - \hat{y}_{ji}| \quad (2)$$

We combine two losses: heatmap loss and counter loss for the supervision of the network $\mathcal{L} = L_{hm} + L_{count}$.

5 Performance Optimizations of CounterNet

To further enhance CounterNet's performance, we introduce a partition-based approach that divides the point cloud into smaller regions, improving counting accuracy (in Section 5.1). Additionally, we propose adding overlap between partitions to more accurately detect objects near the partition boundaries, leading to more precise and reliable counting results (in Section 5.2). We also provide a model selection method to dynamically select the model trained with different parameters to further optimize the counting accuracy across different object type (in Section 5.3).

5.1 CounterNet with Feature Map Partition

Although CounterNet performs well overall, it struggles when there are dense objects in a single frame, which is consistent with the previous findings in images that counting a higher number of objects is inherently more difficult than counting fewer [7, 41]. Additionally, one of the reasons for this difficulty is the imbalance in the training dataset: frames with many objects are underrepresented, while most frames contain only a few or no objects at all. This imbalance makes it harder for the model to generalize well to scenes with a higher object count. To address this issue and improve CounterNet's performance in cases where dense objects are present, we propose CounterNet with partitioning. This method is designed

¹<https://mathworks.com/help/matlab/ref/islocalmax2.html>

to handle high object density cases more effectively, allowing for more accurate counting in complex frames.

Network Architecture. We evenly partition the feature map into regions of equal size. We denote the number of partitions as pt . For example, Figure 4 illustrates the case where $pt = 4$, resulting in four equally sized regions within the feature map. Each region is then passed through convolutional layers to produce a partial heatmap corresponding to that region.

This approach offers several advantages. First, by breaking the feature map into smaller regions, we reduce the object number in each partition. It lowers the complexity of detecting and counting objects within partitions. Second, partitioning increases the amount of effective training data by generating more object-containing regions. By assigning more weight to the loss in data-rich regions, we improve the precision of heatmap generation, ultimately enhancing the overall accuracy of counting.

Dynamic Thresholding for Peak Detection. Once a heatmap is generated from the partitions, using a single threshold for all partitions no longer yields optimal results. For instance, in a large heatmap, high-density partitions tend to have higher overall values, while low-density partitions have lower values. A single threshold applied to all partitions cannot account for these variations, resulting in suboptimal performance.

To address this, we apply Otsu’s method [37] during the inference stage to dynamically determine the optimal threshold k for each partition.

Otsu’s method maximizes the between-class variance, given by the formula: $\alpha_B^2(k) = \omega_0(k) \times \omega_1(k) \times [mean_0(k) - mean_1(k)]^2$. Here, $\omega_0(k)$ and $\omega_1(k)$ are the proportion of points below and above the threshold, respectively, while $mean_0(k)$ and $mean_1(k)$ represent the mean values of the points below and above k , respectively. By maximizing this function, we find the optimal threshold k for each partition. The computed threshold k is then used to distinguish relevant and irrelevant regions within the partition. We combine this dynamic threshold k with the fixed threshold t in training. If $k \geq t$, we adopt k as the threshold for partition, otherwise, we use t as the threshold.

Loss. Since partitioning the feature map introduces imbalance across partitions. To mitigate this, we apply weights to the count loss for each partition, as shown in Equation 3, allowing the model to focus more on high-density partitions.

$$L_{count} = \sum_{i=1}^{|R|} w_i \cdot l_{count}(r_i), w_i = \frac{1}{|R|} + \frac{|r_i.objs|}{\sum_{i=1}^{|R|} |r_i.objs|} \quad (3)$$

Our weight has two parts: the base weight and the counter weight. The base weight, $\frac{1}{|R|}$, is uniformly assigned to all partitions, where $|R|$ is the total number of partitions. The counter weight, $\frac{|r_i.objs|}{\sum_{i=1}^{|R|} |r_i.objs|}$, is calculated according to the number of objects in each partition. Here, $|r_i.objs|$ is the number of objects in the partition, while $\sum_{i=1}^{|R|} |r_i.objs|$ is the total objects across all partitions.

5.2 Feature Map Partition with Overlaps

While partitioning improves counting accuracy in high-density frames, we find that it can sometimes split a single object across multiple partitions, leading to the loss of tracking for that object.

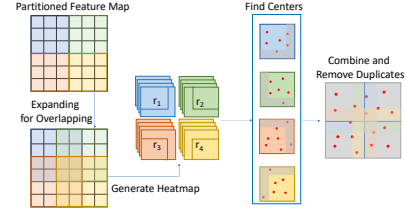


Figure 5: Feature Map Partition with Overlap

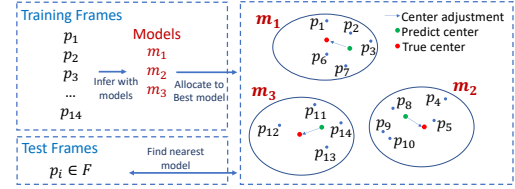


Figure 6: Process of Model Selection

This raises a key question: how do we handle cases where an object’s center falls near the boundary of a partition?

An intuitive approach to prevent objects from being split across partitions is to use feature-based clustering methods such as K-Means [12]. However, clustering presents several challenges in this context. First, it is computationally expensive and struggles to differentiate objects in high-density frames, where object boundaries may be unclear. Second, clustering does not provide guarantees on the shape of partitions, which can result in irregular regions that disrupt backpropagation during training. These limitations make clustering an impractical solution for integrating partitioning into deep learning models.

To overcome these challenges, we propose a simpler and more effective alternative by expanding partition regions to introduce overlap (we use o to represent the expanding ratio), as illustrated in Figure 5. This approach reduces the likelihood of splitting an object across partitions by ensuring that if an object’s center falls near a partition boundary, it is also captured within the central region of an adjacent partition. Compared to clustering, this method has several advantages: (1) it is lightweight and adds minimal computational overhead while preserving the benefits of partitioning, and (2) it integrates seamlessly into the CounterNet pipeline, maintaining consistency across frames.

The training and inference details for CounterNet with overlapped partition can be found in Appendix D.1.

5.3 Query Optimization by Model Selection

Autonomous vehicle point cloud frames vary significantly, making object counting challenging for models with fixed partitions and overlap ratios. Small, numerous objects benefit from more partitions, while larger objects require fewer. We propose a model selection method that chooses the nearest model based on feature distance. To mitigate errors in model center estimation, we apply the Chernoff bound to adjust selection probabilistically. The algorithm can be found in Appendix 2.

Model Center Representation. Given a set of models, denoted as $m \in M$, each corresponding to different partition numbers and overlap ratios, we perform inference on every point cloud frame p in the training dataset using all models in M . For each point cloud frame, we identify the model that demonstrates the best performance. For instance, as shown in Figure 11, the training point cloud frames are allocated to the models as follows: m_1 performs best on $p_1, p_2, p_3, p_6, p_7, m_2$ performs best on $p_4, p_5, p_8, p_9, p_{10}$, and m_3 performs best on $p_{11}, p_{12}, p_{13}, p_{14}$.

For each model m_j , we estimate its center feature, represented as $\hat{\omega}_{m_j}$, by calculating the average feature vector across all point cloud frames associated with the model. The center estimate is computed as: $\hat{\omega}_{m_j} = \frac{1}{n} \sum_{i=0}^n p_i \cdot f$ where $p_i \cdot f$ denoted the feature vector of point cloud frame p_i , and n is the number of point cloud frames associated with model m_j .

Center Adjustment with Confidence. Under the assumption of unlimited data for each $m \in M$, we would ideally obtain the true center μ for each model. However, in practice, data distribution across models is often uneven, making it necessary to estimate the probability of deviation between the evaluated center $\hat{\omega}_{m_j}$ and the true center μ .

To quantify the probability of deviation, we assume point cloud frames are independent and apply the Chernoff bound [16], which provides an upper bound on the probability that $\hat{\omega}_{m_j}$ deviates from μ by more than a given margin ϵ : $P(|\hat{\omega}_{m_j} - \mu| > \epsilon) \leq \exp(-\frac{n\epsilon^2}{2\xi^2})$.

Here, ϵ is the expected deviation, ξ is the sample variance, and n is the number of samples. In this equation, ϵ is the distance threshold defined by the user. Lower ϵ provides a higher probability. This probability P_{m_j} quantifies our confidence in the estimated center $\hat{\omega}_{m_j}$, guiding adjustments to improve model selection.

Find the optimal model. During validation, for each new frame p , we compute the distance between p and the center of each model $m \in M$. The model with the shortest distance to the new point cloud frame is selected for further processing. Additionally, when selecting the closest model center, we must take into account the potential deviation of each model's estimated center from its true center. For the distance between p to each $m \in M$, we combine the distance with the probability: $d_{adjusted}(p, m_j) = d(p, \hat{\omega}_{m_j}) \times P_{m_j}$, where $d(p, \hat{\omega}_{m_j})$ is the distance between p and $\hat{\omega}_{m_j}$, and P_{m_j} is the confidence probability derived from the Chernoff bound. By incorporating P_{m_j} , we adjust for potential deviation in the estimated center and improve robustness in model selection.

6 Experiment

6.1 Experiment Setup

All experiments were conducted on a server running Ubuntu 22.04.1, with Intel(R) Xeon(R) CPU E5-2697A v4 @ 2.60GHz and RTX3080. The code is implemented with OpenPCDet Framework [45]. Our code is available at [1].

Datasets. Experiments are conducted on the nuScenes [5], KITTI [4] and Waymo-partial [42] (detailed explanation in Appendix G).

Methods for Comparison. As explained in Section 2, unlike prior querying studies that focus on indexing [3, 20, 21, 30], our solution focuses on facilitating querying performance by improving object

counting. As a result, we use the following **detection models as our baselines** for querying.

- (1) VoxelNeXt [9] (VN): We use VoxelNeXt, which relies on sparse voxel features to facilitate detection.
- (2) TransFusion [2] (TF): TransFusion utilizes an attention mechanism to fuse point cloud and image data for improved detection.
- (3) CenterPoint [49] (CP): CenterPoint is the pioneer study of the center-based detection model.

Given the availability of baseline implementations on different datasets, we use VoxelNeXt and TransFusion as baselines for the nuScenes dataset. For the Waymo dataset, we adopt VoxelNeXt, while for the KITTI dataset, we use CenterPoint as the baseline.

We also have **our methods** for comparison:

- (1) CounterNet (CN): Our proposed baseline in Section 4.
- (2) CounterNet with partition (CN_{pt}): Our proposed solution, as introduced in Section 5.1.
- (3) CounterNet with overlapped partition (CN_{pt}^o): Our proposed solution, as introduced in Section 5.2.

Evaluation Metrics. We evaluate our approach based on two main aspects: query accuracy and counting performance.

(1) RETRIEVAL. We experimented with two types of retrieval queries: RETRIEVAL-SINGLE and RETRIEVAL-MULTIPLE. These queries retrieve frames containing a specific number of objects. In most analytical scenarios—such as congestion detection—precise object counts are not strictly necessary; instead, a degree of deviation is acceptable to account for natural variability. To evaluate performance, we calculated the percentage of frames in which the retrieval condition was correctly met, allowing for 10% and 5% error tolerance. Since the number of objects in a frame can vary significantly (e.g., some frames contain over 50 cars, while others have at most 20 trucks, as shown in Table 11), we set the error tolerance per category proportionally. Specifically, the tolerance threshold for each object category is determined by multiplying the maximum number of that object type in a scene by the error tolerance. This approach ensures a fair evaluation across categories.

(2) COUNT. The COUNT query counts the number of frames that satisfy a specific condition, such as counting the frames containing 5 cars. To evaluate this, we randomly select 500 groups of consecutive frames with lengths ranging from 100 to 500. For each object category, we generate 1000 random queries requesting different object numbers (not exceeding the maximum number of objects present in any frame) and evaluate the percentage of counts being returned correctly. We allow a 10% error tolerance in the results.

(3) AGGREGATION. The Aggregation query provides statistical information, such as the total number of objects in a set of frames. We evaluate this using the SUM() operation. For random consecutive frame groups of lengths between 100 and 500, we calculate the sum of the queried objects and compare the evaluated sum to the ground truth across 1000 random queries. We use two metrics to evaluate the results: absolute difference and Q-error. The

Notation	Description
CN	CounterNet baseline without partitioning.
CN_{pt}	CounterNet with partitioning. The default setting uses 4 partitions unless otherwise specified.
CN_{pt}^o	CounterNet with partitioning and overlap. Uses the expansion ratio of 0.2 by default.

Table 1: Notations for all tables and figures

		RETRIEVAL-S (10% tolerance)			RETRIEVAL-S (5% tolerance)			AGG (absolute)			AGG (Q-error)		
		nuScenes	KITTI	Waymo	nuScenes	KITTI	Waymo	nuScenes	KITTI	Waymo	nuScenes	KITTI	Waymo
baselines	VN	0.829	–	0.779	0.706	–	0.671	2.637	–	8.884	1.804	–	1.268
	TF	0.857	–	–	0.767	–	–	2.706	–	–	1.774	–	–
	CP	–	0.917	–	–	0.828	–	–	0.330	–	–	1.286	–
ours	CN	0.901	0.939	0.812	0.823	0.846	0.711	1.228	0.189	6.391	1.416	1.080	1.248
	CN_{pt}	0.878 \downarrow	0.935 \downarrow	0.818	0.829	0.840 \downarrow	0.630 \downarrow	1.053	2.501 \uparrow	3.560	1.428 \uparrow	1.067	1.199
	CN_{pt}^o	0.916	0.954	0.846	0.839	0.859	0.712	0.744	0.276	3.301	1.321	1.051	1.197

\downarrow indicates a performance drop for RETRIEVAL, while \uparrow means a performance drop for AGG, compared to CN. Bold indicates the best performance.

Table 2: Overall query result of RETRIEVAL-SINGLE and AGGREGATION

Combinations	VN	TF	CN	CN_{pt}	CN_{pt}^o
(car, pedestrian)	0.582	0.425	0.700	0.800	0.842
(car, barrier)	0.616	0.506	0.693	0.808	0.852
(pedestrian, barrier)	0.568	0.540	0.783	0.791 \downarrow	0.787
(car, pedestrian, barrier)	0.474	0.372	0.623	0.724	0.759
(truck, bus)	0.725	0.605	0.771	0.758 \downarrow	0.828
(bus, trailer)	0.844	0.890	0.910	0.897 \downarrow	0.913
(truck, trailer)	0.732	0.607	0.791	0.773 \downarrow	0.832
(truck, bus, trailer)	0.684	0.591	0.760	0.733 \downarrow	0.804

\downarrow indicates a performance drop compared to CN.

Table 3: RETRIEVAL-MULTIPLE (nuScenes)

	CP	CN	CN_{pt}	CN_{pt}^o
(car, pedestrian)	0.812	0.856	0.854 \downarrow	0.902
(car, cyclist)	0.885	0.887	0.880 \downarrow	0.903
(pedestrian, cyclist)	0.833	0.886	0.868 \downarrow	0.926
(car, pedestrian, cyclist)	0.776	0.821	0.811 \downarrow	0.869

Table 4: ETRIEVAL-MULTIPLE (KITTI)

	VN	CN	CN_{pt}	CN_{pt}^o
(vehicle, pedestrian)	0.757	0.798	0.748 \downarrow	0.835
(vehicle, cyclist)	0.751	0.792	0.733 \downarrow	0.832
(pedestrian, cyclist)	0.757	0.790	0.748 \downarrow	0.831
(vehicle, pedestrian, cyclist)	0.745	0.780	0.692 \downarrow	0.818

Table 5: RETRIEVAL-MULTIPLE (Waymo)

		COUNT		
		nuScenes	KITTI	Waymo
baselines	VN	0.658	–	0.763
	TF	0.683	–	–
	CP	–	0.771	–
ours	CN	0.759	0.7959	0.779
	CN_{pt}	0.791	0.780	0.771
	CN_{pt}^o	0.857	0.846	0.807

Table 6: Overall query result of COUNT

absolute difference measures the average deviation between the predicted and ground truth sums, providing a straightforward sense of numerical accuracy. In contrast, Q-error (quantile error) evaluates the ratio between the predicted and actual values, capturing the relative error, which is used widely in cardinality analysis for database [13]. Specifically, it is defined as the maximum of the ratio between the prediction and the ground truth, and vice versa, i.e., $Q\text{-error} = \max\left(\frac{\hat{y}}{y}, \frac{y}{\hat{y}}\right)$. Within the 1000 queries, we take the median as our reported Q-error.

Notation and Parameter Setting. Please refer to Table 1 for the notation of different CounterNet variants and the default values.

6.2 Effectiveness Study on Various Query Types

Table 2 and Table 6 demonstrate the overall performance of the three query types: RETRIEVAL, AGGREGATION, and COUNT. Across all three queries, the partition-based model (CN_{pt}) does not consistently outperform the baseline (CN), with performance drops particularly obvious on the KITTI dataset in both *RETRIEVAL-SINGLE* (i.e., *RETRIEVAL-S*) and *AGGREGATION* (i.e. *AGG*) queries. This decline is likely due to KITTI’s smaller spatial coverage per point

cloud frame, making it more sensitive to partitioning. However, introducing overlap in the partitioning strategy (CN_{pt}^o) effectively mitigates this issue, delivering the best performance in most cases and demonstrating greater robustness across datasets of varying scales. Although all models exhibit decreased *RETRIEVAL* performance under the stricter 5% error tolerance, the degradation is more pronounced in CN_{pt} , while CN_{pt}^o remains comparatively stable, further highlighting its resilience.

Table 3 - Table 5 show RETRIEVAL-MULTIPLE results on different datasets. In table 3, we evaluate two groups based on occurrence frequency: high-frequency objects (cars, pedestrians, barriers) and low-frequency objects (trucks, buses, trailers), by referring to Table 11 for object frequency on nuScenes in Appendix E. (1) High-Frequency Objects: Partitions enhance the result, and overlap further improves it, except for pedestrians and barriers, where duplicate counts in overlapped regions reduce accuracy due to their smaller size and higher occurrence rates. (2) Low-Frequency Objects: Partitions do not improve the accuracy, but overlap significantly enhances performance, particularly for sparsely distributed or large objects. For the detailed categorical results and analysis can be found in Appendix E - G.

6.3 Parameter Study

(1) Partitioning without Overlap (CN_{pt}): As shown in Figure 7, increasing the number of partitions generally degrades performance for larger objects such as trucks and buses, likely due to their increased probability of being segmented. Conversely, smaller objects

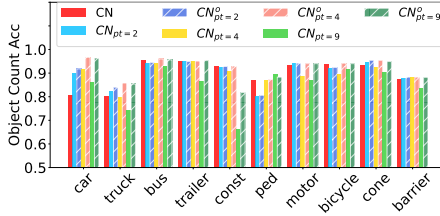


Figure 7: Different Partitions(nuScenes)

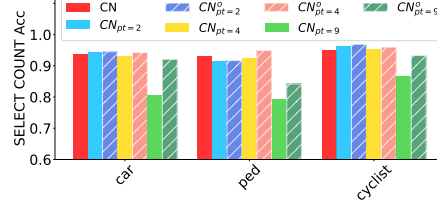


Figure 8: Different partitions(KITTI)

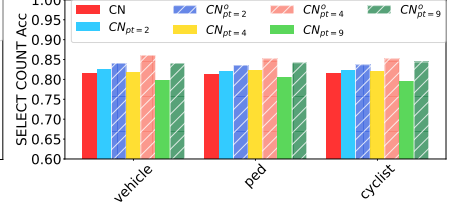


Figure 9: Different partitions(Waymo)

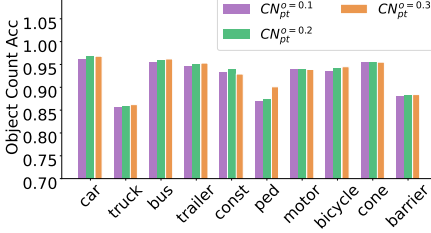


Figure 10: Different overlaps(nuScenes)

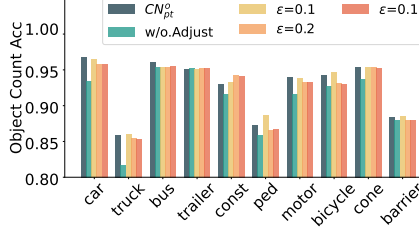


Figure 11: Model selection(nuScenes)

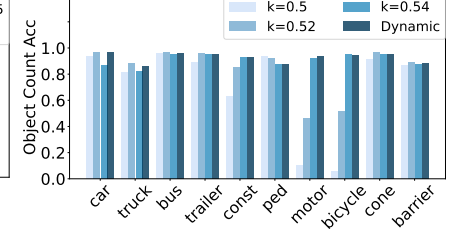


Figure 12: Thresholding(nuScenes)

like pedestrians benefit from an increased number of partitions. Notably, performance declines sharply with nine partitions, indicating a negative effect on accuracy for most object categories.

(2) Partitioning with Overlap (CN_{pt}^o): As shown in Figure 7, the overlap can mitigate the negative impacts of partitioning. In most cases, with overlaps, the partitions enhance performance, particularly as the number of partitions increases. The benefits are obvious with 9 partitions compared with 2 partitions.

(3) Increasing Overlap Ratio: As demonstrated in Figure 10, increasing the expansion ratio contributes little to the improvement of query accuracy. This finding indicates that while overlap helps, its benefits are not substantial by blind expansion.

Both Waymo and nuScenes provide 360° scenes, but Waymo covers a larger range (150.4m) compared to nuScenes (102.4m). In contrast, the KITTI dataset only captures a forward-facing view, with a range of 70.4m × 80m. Considering the differences in dataset scale, we analyze the impact of partitioning on query results across these datasets. As shown in Figure 8 and Figure 9, Waymo, with its larger scene scale, tends to benefit more from partitioning and overlaps. In contrast, KITTI, which has a smaller scene scale, experiences a performance drop when using 9 partitions, which cannot be mitigated by overlap.

6.4 Efficiency Study

Table 7 presents per-frame processing times (in seconds) across three datasets: nuScenes, KITTI, and Waymo, for different model

	CN	$CN_{pt=2}$	$CN_{pt=2}^o$	$CN_{pt=4}$	$CN_{pt=4}^o$	$CN_{pt=9}$	$CN_{pt=9}^o$
nuScenes	152	155	160	165	172	184	189
KITTI	100	101	104	103	105	104	107
Waymo	112	113	115	114	121	114	128

Table 7: Processing time per frame in milliseconds

Model		w/o.Adjust	$\epsilon = 0.1$		$\epsilon = 0.15$		$\epsilon = 0.2$	
pt	o	dist	rate	dist	rate	dist	rate	dist
2	0	1116	0.835	339	0.667	168	0.486	90
2	0.1	21	0.780	279	0.572	274	0.371	343
2	0.2	48	0.811	43	0.624	35	0.433	32
4	0	9	0.543	556	0.379	743	0.087	752
4	0.1	14	0.650	9	0.379	7	0.178	8
4	0.2	4739	0.617	4736	0.337	4734	0.145	4735
9	0	20	0.642	0	0.426	3	0.219	3
9	0.1	34	0.693	48	0.369	53	0.170	54
9	0.2	16	0.684	7	0.439	35	0.231	0

Table 8: Data distribution (abbr. dist) of model selection with adjustment with 9 models (nuScenes)

variants. Overall, processing time increases gradually from the baseline (CN) to more complex variants ($CN_{pt=2}$, $CN_{pt=4}$, $CN_{pt=9}$) and their optimized versions ($CN_{pt=2}^o$, $CN_{pt=4}^o$, $CN_{pt=9}^o$). Furthermore, on the nuScenes dataset, our method achieves comparable processing time to the baselines: 201 ms for TF and 154 ms for VN. While our solution yields similar results in terms of inference time, it demonstrates the advantage in effectiveness as discussed above.

6.5 Study of Model Selection

Table 8 shows model selection results based on data distribution (i.e., frame allocation) with ϵ values from 0.1 to 0.2, where higher ϵ indicates a tighter bound. Key observations: (1) Model $CN_{pt=2}^{o=0.2}$ dominates, but frame allocation varies with adjustment. Without adjustment, many frames (e.g., 1116) are inefficiently allocated to suboptimal model $CN_{pt=2}^{o=0}$, while adjustment reallocates frames to more reliable models like $CN_{pt=2}^{o=0.1}$ (better for larger objects like buses), $CN_{pt=4}^{o=0}$, and $CN_{pt=9}^{o=0.1}$ (better for smaller objects like pedestrians). (2) Lower ϵ increasing adjustment rates and true center

deviations, while larger ϵ reduce adjustment influence; a balance is crucial. The selection of ϵ can be found in Appendix E.3 (3) Evaluation via object count accuracy (Figure 11) using $CN_{pt=4}^{o=0.2}$ as the baseline shows that, without model selection, performance worsens due to $CN_{pt=2}^{o=0}$. Adjustments improve balance across categories, trading $CN_{pt=4}^{o=0.2}$'s exceptional detection of cars and buses for gains in detecting pedestrians, bicycles, and barriers. For more experiments of the model selection, see Appendix E.3.

7 Conclusion

In this paper, we present CounterNet, a method to facilitate querying 3D point cloud data with a focus on accurate object counting. By emphasizing object appearance detection and introducing a partition-based strategy with overlapping regions, we improve performance across varying object densities. Additionally, our dynamic model selection ensures robustness across scenarios. Experiments show that our approach enhances object counting accuracy, thereby improving query effectiveness. In the future, this research can be extended in several directions: (1) Investigating more efficient solutions for querying point cloud data, optimizing both performance and scalability. (2) Leveraging the query tool to support data acquisition research, enabling the extraction of relevant data from a data pool to enhance model training for specific tasks.

References

- [1] Authors. 2025. Code. <https://github.com/PetalZh/PCQuery>.
- [2] Xuyang Bai, Zeyu Hu, Xinge Zhu, Qingqiu Huang, Yilun Chen, Hongbo Fu, and Chiew-Lan Tai. 2022. Transfusion: Robust lidar-camera fusion for 3d object detection with transformers. In *CVPR*. 1090–1099.
- [3] Jaeho Bang, Gaurav Tarlok Kakkar, Pramod Chunduri, Subrata Mitra, and Joy Arulraj. 2023. Seiden: Revisiting Query Processing in Video Database Systems. *VLDB* 16, 9 (2023), 2289–2301.
- [4] J. Behley, M. Garbade, A. Milioto, J. Quenzel, S. Behnke, C. Stachniss, and J. Gall. 2019. SemanticKITTI: A Dataset for Semantic Scene Understanding of LiDAR Sequences. In *ICCV*.
- [5] Holger Caesar, Varun Bankiti, Alex H. Lang, Sourabh Vora, Venice Erin Liong, Qiang Xu, Anush Krishnan, Yu Pan, Giancarlo Baldan, and Oscar Beijbom. 2019. nuScenes: A multimodal dataset for autonomous driving. *arXiv preprint arXiv:1903.11027* (2019).
- [6] Jia Shen Cao, Karan Sarkar, Ramyad Hadidi, Joy Arulraj, and Hyesoon Kim. 2022. Figo: Fine-grained query optimization in video analytics. In *SIGMOD*. 559–572.
- [7] Prithvijit Chattopadhyay, Ramakrishna Vedantam, Ramprasaath R Selvaraju, Dhruv Batra, and Devi Parikh. 2017. Counting everyday objects in everyday scenes. In *CVPR*. 1135–1144.
- [8] Xiaozhi Chen, Huimin Ma, Ji Wan, Bo Li, and Tian Xia. 2017. Multi-view 3d object detection network for autonomous driving. In *CVPR*. 1907–1915.
- [9] Yukang Chen, Jianhui Liu, Xiangyu Zhang, Xiaojuan Qi, and Jiaya Jia. 2023. Voxelnext: Fully sparse voxelnet for 3d object detection and tracking. In *CVPR*. 21674–21683.
- [10] Hisham Cholakkal, Guolei Sun, Salman Khan, Fahad Shahbaz Khan, Ling Shao, and Luc Van Gool. 2020. Towards partial supervision for generic object counting in natural scenes. *IEEE Transactions on Pattern Analysis and Machine Intelligence* 44, 3 (2020), 1604–1622.
- [11] Mehmet Emin Dönderler, Ediz Şaykol, Umut Arslan, Özgür Ulusoy, and Uğur Gündükbay. 2005. BilVideo: Design and implementation of a video database management system. *Multimedia Tools and Applications* 27, 1 (2005), 79–104.
- [12] Vance Faber et al. 1994. Clustering and the continuous k-means algorithm. *Los Alamos Science* 22, 138144.21 (1994), 67.
- [13] Yuxing Han, Ziniu Wu, Peizhi Wu, Rong Zhu, Jingyi Yang, Liang Wei Tan, Kai Zeng, Gao Cong, Yanzhao Qin, Andreas Pfadler, Zhengping Qian, Jingren Zhou, Jiangneng Li, and Bin Cui. 2021. Cardinality Estimation in DBMS: A Comprehensive Benchmark Evaluation. *Proc. VLDB Endow.* 15, 4 (2021), 752–765.
- [14] Kaiming He, Georgia Gkioxari, Piotr Dollár, and Ross Girshick. 2017. Mask r-cnn. In *ICCV*. 2961–2969.
- [15] Kaiming He, Xiangyu Zhang, Shaoqing Ren, and Jian Sun. 2016. Deep residual learning for image recognition. In *CVPR*. 770–778.
- [16] Martin Hellman and Josef Raviv. 1970. Probability of error, equivocation, and the Chernoff bound. *IEEE Transactions on Information Theory* 16, 4 (1970), 368–372.
- [17] Porter Jenkins, Kyle Armstrong, Stephen Nelson, Siddhesh Gotad, J Stockton Jenkins, Wade Wilkey, and Tanner Watts. 2023. Countnet3d: A 3d computer vision approach to infer counts of occluded objects. In *Proceedings of the IEEE/CVF Winter Conference on Applications of Computer Vision*. 3008–3017.
- [18] Ruixiang Jiang, Lingbo Liu, and Changwen Chen. 2023. Clip-count: Towards text-guided zero-shot object counting. In *Proceedings of the 31st ACM International Conference on Multimedia*. 4535–4545.
- [19] Glenn Jocher, Alex Stoken, Jirka Borovec, NanoCode012, ChristopherSTAN, Liu Changyu, Laughing, tkianai, Adam Hogan, lorenzomammama, yxNONG, AlexWang1900, Laurentiu Diaconu, Marc, wanghaoyang0106, ml5ah, Doug, Francisco Ingham, Frederik, Guillen, Hatovix, Jake Poznanski, Jiacong Fang, Lijun Yu, changyu98, Mingyu Wang, Naman Gupta, Osama Akhtar, PetrDvoracek, and Prashant Rai. 2020. *ultralytics/yolov5: v3.1*. doi:10.5281/zenodo.4154370
- [20] Daniel Kang, Peter Bailis, and Matei Zaharia. 2019. BlazeIt: Optimizing Declarative Aggregation and Limit Queries for Neural Network-Based Video Analytics. *VLDB* 13, 4 (2019).
- [21] Daniel Kang, John Guibas, Peter D Bailis, Tatsunori Hashimoto, and Matei Zaharia. 2022. Tasti: Semantic indexes for machine learning-based queries over unstructured data. In *SIGMOD*. 1934–1947.
- [22] Seunggu Kang, WonJun Moon, Euiyeon Kim, and Jae-Pil Heo. 2024. Vlcounter: Text-aware visual representation for zero-shot object counting. In *Proceedings of the AAAI Conference on Artificial Intelligence*, Vol. 38. 2714–2722.
- [23] Fiodar Kazhamiaka, Matei Zaharia, and Peter Bailis. 2021. Challenges and Opportunities for Autonomous Vehicle Query Systems.. In *CIDR*.
- [24] Xin Lai, Yukang Chen, Fanbin Lu, Jianhui Liu, and Jiaya Jia. 2023. Spherical transformer for lidar-based 3d recognition. In *CVPR*. 17545–17555.
- [25] Alex H Lang, Sourabh Vora, Holger Caesar, Lubing Zhou, Jiong Yang, and Oscar Beijbom. 2019. Pointpillars: Fast encoders for object detection from point clouds. In *CVPR*. 12697–12705.
- [26] Issam H Laradji, Negar Rostamzadeh, Pedro O Pinheiro, David Vazquez, and Mark Schmidt. 2018. Where are the blobs: Counting by localization with point supervision. In *ECCV*. 547–562.

- [27] Hei Law and Jia Deng. 2018. Cornernet: Detecting objects as paired keypoints. In *ECCV*. 734–750.
- [28] Thi-Lan Le, Monique Thonnat, Alain Boucher, and François Brémont. 2008. A query language combining object features and semantic events for surveillance video retrieval. In *International Conference on Multimedia Modeling*. Springer, 307–317.
- [29] Asad Lesani, Ehsan Nateghinia, and Luis F Miranda-Moreno. 2020. Development and evaluation of a real-time pedestrian counting system for high-volume conditions based on 2D LiDAR. *Transportation research part C: emerging technologies* 114 (2020), 20–35.
- [30] Jiangneng Li, Haitao Yuan, Gao Cong, Han Mao Kiah, and Shuhao Zhang. 2025. MAST: Towards Efficient Analytical Query Processing on Point Cloud Data. *Proceedings of the ACM on Management of Data* 3, 1 (2025), 1–27.
- [31] Tsung-Yi Lin, Priya Goyal, Ross Girshick, Kaiming He, and Piotr Dollár. 2017. Focal loss for dense object detection. In *ICCV*. 2980–2988.
- [32] Shaoshan Liu, Liangkai Liu, Jie Tang, Bo Yu, Yifan Wang, and Weisong Shi. 2019. Edge computing for autonomous driving: Opportunities and challenges. *Proc. IEEE* 107, 8 (2019), 1697–1716.
- [33] Zhijian Liu, Haotian Tang, Shengyu Zhao, Kevin Shao, and Song Han. 2021. Pvnas: 3d neural architecture search with point-voxel convolution. *IEEE Transactions on Pattern Analysis and Machine Intelligence* 44, 11 (2021), 8552–8568.
- [34] Chenglang Lu, Mingyong Liu, and Zongda Wu. 2015. Svql: A sql extended query language for video databases. *International Journal of Database Theory and Application* 8, 3 (2015), 235–248.
- [35] Guo Ming. 2023. Exploration of the intelligent control system of autonomous vehicles based on edge computing. *PLoS One* 18, 2 (2023), e0281294.
- [36] Anjana K Nellithimaru and George A Kantor. 2019. Rols: Robust object-level slam for grape counting. In *CVPR workshops*. 0–0.
- [37] Nobuyuki Otsu et al. 1975. A threshold selection method from gray-level histograms. *Automatica* 11, 285–296 (1975), 23–27.
- [38] Charles R Qi, Hao Su, Kaichun Mo, and Leonidas J Guibas. 2017. Pointnet: Deep learning on point sets for 3d classification and segmentation. In *CVPR*. 652–660.
- [39] Charles Ruizhongtai Qi, Li Yi, Hao Su, and Leonidas J Guibas. 2017. Pointnet++: Deep hierarchical feature learning on point sets in a metric space. *NeurIPS* 30 (2017).
- [40] Shaoshuai Shi, Chaoxu Guo, Li Jiang, Zhe Wang, Jianping Shi, Xiaogang Wang, and Hongsheng Li. 2020. Pv-rcnn: Point-voxel feature set abstraction for 3d object detection. In *CVPR*. 10529–10538.
- [41] Tobias Stahl, Silvia L Pintea, and Jan C Van Gemert. 2018. Divide and count: Generic object counting by image divisions. *IEEE Transactions on Image Processing* 28, 2 (2018), 1035–1044.
- [42] Pei Sun, Henrik Kretzschmar, Xerxes Dotiwalla, Aurelien Chouard, Vijaysai Patnaik, Paul Tsui, James Guo, Yin Zhou, Yuning Chai, Benjamin Caine, Vijay Vasudevan, Wei Han, Jiquan Ngiam, Hang Zhao, Aleksei Timofeev, Scott Ettinger, Maxim Krivokon, Amy Gao, Aditya Joshi, Yu Zhang, Jonathon Shlens, Zhifeng Chen, and Dragomir Anguelov. 2020. Scalability in Perception for Autonomous Driving: Waymo Open Dataset. In *CVPR*.
- [43] Pei Sun, Mingxing Tan, Weiyue Wang, Chenxi Liu, Fei Xia, Zhaoqi Leng, and Dragomir Anguelov. 2022. SWFormer: Sparse Window Transformer for 3D Object Detection in Point Clouds. In *ECCV*, Shai Avidan, Gabriel J. Brostow, Moustapha Cissé, Giovanni Maria Farinella, and Tal Hassner (Eds.), Vol. 13670. Springer, 426–442.
- [44] Sihai Tang, Bruce Chen, Harold Iwen, Jason Hirsch, Song Fu, Qing Yang, Paparao Palacharla, Nannan Wang, Xi Wang, and Weisong Shi. 2021. Vecframe: A vehicular edge computing framework for connected autonomous vehicles. In *2021 IEEE International Conference on Edge Computing (EDGE)*. IEEE, 68–77.
- [45] OpenPCDet Development Team. 2020. OpenPCDet: An Open-source Toolbox for 3D Object Detection from Point Clouds. <https://github.com/open-mmlab/OpenPCDet>.
- [46] Jingyi Xu, Hieu Le, Vu Nguyen, Viresh Ranjan, and Dimitris Samaras. 2023. Zero-shot object counting. In *CVPR*. 15548–15557.
- [47] Yan Yan, Yuxing Mao, and Bo Li. 2018. Second: Sparsely embedded convolutional detection. *Sensors* 18, 10 (2018), 3337.
- [48] Zetong Yang, Yanan Sun, Shu Liu, and Jiaya Jia. 2020. 3dssd: Point-based 3d single stage object detector. In *CVPR*. 11040–11048.
- [49] Tianwei Yin, Xingyi Zhou, and Philipp Krähenbühl. 2021. Center-based 3d object detection and tracking. In *CVPR*. 11784–11793.
- [50] Hui Zhou, Xinge Zhu, Xiao Song, Yuexin Ma, Zhe Wang, Hongsheng Li, and Dahua Lin. 2020. Cylinder3d: An effective 3d framework for driving-scene lidar semantic segmentation. *arXiv preprint arXiv:2008.01550* (2020).
- [51] Xingyi Zhou, Vladlen Koltun, and Philipp Krähenbühl. 2020. Tracking Objects as Points. In *ECCV*, Andrea Vedaldi, Horst Bischof, Thomas Brox, and Jan-Michael Frahm (Eds.), Vol. 12349. Springer, 474–490.
- [52] Yin Zhou and Oncel Tuzel. 2018. Voxelnet: End-to-end learning for point cloud based 3d object detection. In *CVPR*. 4490–4499.

A Table of Notation

\mathcal{P}	set of point cloud frames
p	point cloud frame
q	query object
op	operations set
ct	object count
Y	GT label for heatmap
\hat{Y}	predicts for heatmap
(x, y)	point coordinate
c	object category
y	GT object count
\hat{y}	predict object count
k	dynamic threshold for heatmap
t	fixed threshold for heatmap
r	feature map region
pt	partition number
o	expanding overlapping ratio
M	set of models
m	model
$\hat{\omega}$	estimated center
μ	true center
ϵ	expected deviation
ξ	sample variance

Table 9: Table of notation

B Motivation Example for the Study

Our study is driven by the need to develop a query tool for point cloud data to address specific tasks. We use a real-world example to further illustrate the importance and necessity of this query tool, reinforcing the motivation behind our research.

Querying specific frames in point cloud data is crucial for facilitating target tasks. For example, to enhance a model’s ability to detect pedestrians, a direct and effective approach is to train or fine-tune the model using frames containing pedestrians rather than relying on the entire dataset. This targeted approach not only improves performance but also reduces computation costs. We conducted a simple experiment using the KITTI dataset. As shown in Figure 10, we compared pedestrian detection performance under three conditions: (1) Training on the full dataset (3712 frames). (2) Training on a randomly sampled subset of 1,000 frames. (3) Training on a carefully selected subset of frames containing pedestrians (about 955 frames).

The results demonstrated that using the carefully selected subset improved pedestrian detection performance, achieving similar or better results compared to the full dataset while reducing training costs by approximately two-thirds.

This experiment highlights the necessity of querying point cloud data, proving its potential to enhance task-specific performance and optimize resource utilization.

C Data Model Design and Explanation for Query Type Selection

C.1 Data Model

As illustrated below, our data model is designed with the NoSQL format, which brought more flexibility in aggregating data from

	Car			Pedestrian			Cyclist		
	Easy	Mod	Hard	Easy	Mod	Hard	Easy	Mod	Hard
Full (3712 frames)	69.42	61.44	58.33	33.88	31.96	31.25	63.47	48.28	46.11
Random (1000 frames)	70.72	60.31	55.56	35.38	33.11	31.91	60.04	44.26	42.57
Pedestrian (955 frames)	70.38	58.38	54.63	37.88	36.11	34.53	59.46	43.81	42.49

Table 10: Detection results of training with different set

different sources, such as different vehicles, making it more suitable for handling the diverse and complex nature of autonomous driving data. Object counting, being one of the most essential pieces of information required for querying [3, 6, 20, 21], shapes the design of our data model, as shown below. We store key information from each frame, including object type, count, and the approximate positions of objects in a bird's eye view, ensuring that the data model is optimized for efficient querying.

```
{ "frame_id": "frame123",
  "timestamp": "2024-04-07 15:43:02.8924030000",
  "vehicle_id": "vehicle_00000000",
  "objects": [
    { "type": "car",
      "count": "10",
      "position": [{"x": 1.5, "y": 2.1}, ...] },
    ... ]
}
```

D Methodology

D.1 Overlapped Partition

The training process and loss calculation follow the same procedure as CounterNet with Partition introduced in Section 5.1. However, the inference process involves additional steps to account for overlapping partitions, as shown in Figure 10 and Algorithm 1: (1) Generate Expanded Partitioned Heatmaps. Given a feature map, we first divide it into partitions (Line 1). Based on the expansion ratio δ , we calculate the required width and height for the expansion (Lines 3-4) and determine the region coordinates with the expanded width and height (Lines 5-8). (2) Extract Centers from Partitions and Merge. We generate the heatmap for each partitioned region (Line 9). Afterward, the centers extracted from each heatmap are merged into a single map (Lines 10-15). (3) Remove Duplicate Center Points. Using a predefined radius γ , we merge centers that fall within this radius (Lines 16-21).

D.2 Model Selection

The overall process of model selection is explained in Algorithm 2, which main contains three steps: (1) Model center representation. (2) Center adjustment with confidence. (3) Find the optimal model.

E Additional Experiments on nuScenes

The nuScenes dataset includes 28,130 samples in the training set and 6,019 samples in the validation set. We train and evaluate the model with 10 categories of objects, including car, truck, construction_vehicle (const), bus, trailer, barrier, motorcycle (moto), bicycle (bicyc), pedestrian (ped), and traffic_cone (cone).

Algorithm 1: Inference with Overlap Partition

Input: feature map F , expanding ratio δ , radius γ
Output: centers

```
1  $R = \text{getPartitions}(F)$ ;
   // Expand regions
2 foreach  $r \in R$  do
3    $\text{expand\_w} = r.\text{width} \times \delta$ ;
4    $\text{expand\_h} = r.\text{height} \times \delta$ ;
5    $r.x_{\text{start}} = \max(0, r.x_{\text{start}} - \text{expand\_w})$ ;
6    $r.y_{\text{start}} = \max(0, r.y_{\text{start}} - \text{expand\_h})$ ;
7    $r.x_{\text{end}} = \min(F.\text{width}, r.x_{\text{end}} + \text{expand\_w})$ ;
8    $r.y_{\text{end}} = \min(F.\text{height}, r.y_{\text{end}} + \text{expand\_h})$ ;
9  $H = \text{getHeatmaps}(R)$ ;
10  $\text{map} = \text{zeros}((F.\text{width}, F.\text{height}))$  // init map of 0
11 foreach  $h \in H$  do
12    $C = \text{getCentersFromHeatmap}(h)$ ;
13   // region coord  $\rightarrow$  map coord
14    $C = \text{transCoordinate}(C)$ ;
15   foreach  $c \in \text{centers}$  do
16      $\text{map}[c.x, c.y] = 1$ 
17   // Combine duplicate centers
18  $\text{centers} = \text{getCenters}(\text{map})$ ;
19  $\text{new\_centers} = \emptyset$ ;
20 while  $\text{centers}$  do
21    $\text{current\_center} = \text{centers.pop}(0)$ ;
22    $\text{new\_centers.add}(\text{current\_c})$ ;
23    $\text{centers} = \text{combineCenters}(\text{centers}, r)$ ;
24 return  $\text{new\_centers}$ 
```

E.1 Data Distribution of Dataset

Table 11 demonstrates the data distribution of the nuScenes dataset. In this table, we present the statistics showing the number of frames that contain a specific number of objects (as indicated in the first row).

E.2 Categorical Query Results

By analyzing the results from RETRIEVAL-SINGLE (Table 12), COUNT and AGGREGATION (Table 13), we observe: (1) CounterNet (CN) Performance: CounterNet outperforms detection models like Vox- elNeXt (VN) and TransFusion (TF), demonstrating its outstanding in extracting query-specific information. (2) Impact of Partitioning: Partitioning improves accuracy for small-object categories like cars and barriers, while performance remains stable for pedestrians. However, it reduces accuracy for larger objects (e.g., trucks, buses) due to increased segmentation across partitions, aligning with our hypothesis that partitioning benefits small or numerous objects but hinders performance for infrequent, large objects. (3) Impact of Overlapping: Overlapped partitions improve performance across all categories, mitigating partitioning drawbacks (e.g., segmentation issues) while maintaining its advantages for counting small or numerous objects.

E.3 Model Selection

Study of ϵ . Figure 16 illustrates how different values of ϵ affect the computed probabilities. Since the center adjustment relies on these

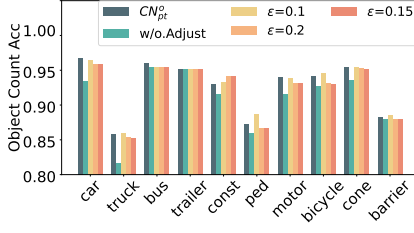


Figure 13: Model selection with 9 models (nuScenes)

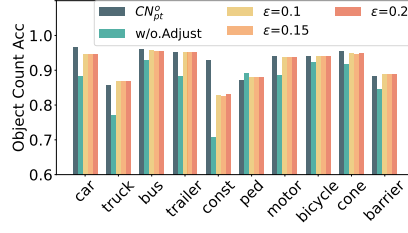


Figure 14: Model selection with 6 models (nuScenes)

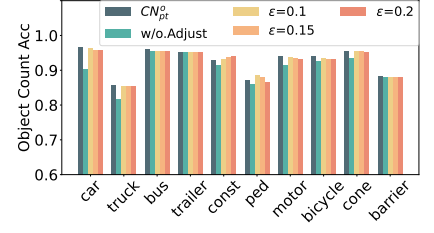


Figure 15: Model selection with emphasis on car & pedestrian (nuScenes)

Algorithm 2: Model Selection

Input: model set M , threshold ϵ , training point cloud set \mathcal{P}_{train} , eval point cloud set \mathcal{P}_{eval}

/* Step 1: Model Center Representation */

/* Initialize assignment sets */

1 Initialize $m.A \leftarrow \emptyset$ for each $m \in M$

2 **foreach** $p \in \mathcal{P}$ **do**

3 $best_model \leftarrow None$;

4 $best_acc \leftarrow -\infty$;

5 **foreach** $m \in M$ **do**

6 $acc \leftarrow \text{EvaluateModel}(m, p)$; // Evaluate model m on p

7 **if** $acc > best_acc$ **then**

8 $best_acc \leftarrow acc$;

9 $best_model \leftarrow m$;

10 $best_model.A \leftarrow best_model.A \cup \{p\}$

/* Step 2: Center Adjustment with Confidence */

11 Initialize $m.\hat{\omega} \leftarrow \emptyset$ and $m.P \leftarrow \emptyset$;

12 **foreach** $m \in M$ **do**

13 /* Number of assigned point clouds */

14 $n \leftarrow |m.A|$

15 /* estimated center */

16 $m.\hat{\omega} \leftarrow \frac{1}{n} \sum_{p \in m.A} p.f$

17 /* sample variance */

18 $\xi^2 \leftarrow \frac{1}{n} \sum_{p \in m.A} (p.f - m.\hat{\omega})^2$

19 /* confidence probability using Chernoff bound */

20 $m.c \leftarrow \exp\left(-\frac{n\epsilon^2}{2\xi^2}\right)$

/* Step 3: Find the optimal model */

21 **foreach** $p \in \mathcal{P}_{val}$ **do**

22 /* Track best model and minimum adjusted distance */

23 Initialize $m^* \leftarrow None$, $d_{min} \leftarrow \infty$

24 **foreach** $m \in M$ **do**

25 /* Euclidean distance */

26 $d \leftarrow \text{ComputeDistance}(p.f, m.\hat{\omega})$

27 /* Adjust distance */

28 $d_{adjusted} \leftarrow d \times m.c$

29 **if** $d_{adjusted} < d_{min}$ **then**

30 $d_{min} \leftarrow d_{adjusted}$; $m^* \leftarrow m$

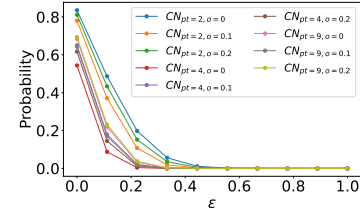
31 $m^*(p)$

probabilities, choosing an appropriate ϵ is crucial. An excessively high ϵ results in probabilities that are too large, diminishing the

# of objects	1-5	6-10	11-15	16-20	21-30	31-40	41-50	≥ 51
car	1953	1794	1070	578	223	69	19	8
pedestrian	2863	724	231	197	113	30	6	12
barrier	463	329	280	190	113	33	16	4
traffic_cone	1408	417	104	48	71	10	1	-
truck	3225	248	63	6	-	-	-	-
bus	1504	12	-	-	-	-	-	-
trailer	818	81	37	6	-	-	-	-
construction_vehicle	1134	-	-	-	-	-	-	-
motorcycle	1192	40	-	-	-	-	-	-

Table 11: Statistic of nuScenes dataset

impact of the adjustment. Conversely, a very low ϵ causes the adjustment to dominate, reducing the influence of the original distance. From the figure, we observe that setting ϵ between 0.1 and 0.2 yields the best results for the nuScenes dataset.

Figure 16: The relationship between ϵ and probability

Our full experiment for evaluating model selection includes: (1) **Evaluation of Different Model Combinations.** We conduct experiments using different combinations of models. The results for 9 models and 6 models are presented in Table 17 and Table 18, respectively. The corresponding counting results are illustrated in Figure 13 and Figure 14. (2) **Weight adjustment for specific categories.** When generating the center of each model, we assign higher weights to the categories of “cars” and “pedestrians”. The results of this adjustment are shown in Table 19, with the corresponding counting performance in Figure 15.

With the experiments, we have the following observations:

(1) **Compare results of using 6 models and 9 models.** Table 18 and Figure 14 show the results of using 6 models for model selection. Compared to the results with 9 models, we removed the dominant models from the 9-model set (i.e., $CN_{pt=4}^{o=0}$, $CN_{pt=4}^{o=0.1}$, and $CN_{pt=4}^{o=0.2}$). According to Table 18, after removing the $CN_{pt=4}$ series models, the new dominant model without adjustment becomes $CN_{pt=9}$. However, with the adjustment, the dominant model shifts to $CN_{pt=9}^{o=0.1}$,

RETRIEVAL-SINGLE(10% tolerance)						RETRIEVAL-SINGLE(5% tolerance)				
	VN	TF	CN	CN_{pt}	CN_{pt}^o	VN	TF	CN	CN_{pt}	CN_{pt}^o
car	0.801	0.615	0.807	0.919	0.967	0.536	0.506	0.601	0.774	0.861
truck	0.778	0.621	0.802	0.799	0.858	0.594	0.610	0.659	0.609↓	0.705
bus	0.917	0.959	0.957	0.944	0.960	0.917	0.959	0.957	0.944↓	0.960
trailer	0.915	0.925	0.953	0.950	0.951	0.815	0.909	0.912	0.880↓	0.871
const	0.845	0.886	0.929	0.910	0.931	0.849	0.886	0.929	0.909↓	0.810
ped	0.711	0.640	0.870	0.869	0.873	0.469	0.553	0.741	0.735↓	0.748
moto	0.728	0.867	0.933	0.886↓	0.940	0.728	0.866	0.933	0.886↓	0.940
bicyc	0.632	0.828	0.940	0.898↓	0.942	0.632	0.907	0.940	0.898↓	0.942
cone	0.706	0.722	0.933	0.926↓	0.954	0.528	0.717	0.875	0.874↓	0.867
barrier	0.761	0.802	0.874	0.883	0.883	0.640	0.755	0.811	0.823	0.824

↓ indicates a performance drop compared to CN.

Table 12: Result of RETRIEVAL-SINGLE (nuScenes)

COUNT						AGG (absolute)					AGG (q-error)				
	VN	TF	CN	CN_{pt}	CN_{pt}^o	VN	TF	CN	CN_{pt}	CN_{pt}^o	VN	TF	CN	CN_{pt}	CN_{pt}^o
car	0.552	0.355	0.947	0.927↓	0.953	4.021	6.488	3.986	2.357	0.662	1.478	1.736	1.401	1.403↑	1.290
truck	0.309	0.431	0.351	0.588	0.592	1.544	2.568	1.157	0.723	0.506	1.979	2.222	1.828	1.842↑	1.522
bus	0.950	0.994	0.859	0.857↓	0.860	0.401	0.220	0.228	0.259	0.183	1.000	1.000	1.113	1.065	1.000
trailer	0.562	0.858	0.787	0.829	0.865	0.786	0.703	0.373	0.355	0.390	1.001	1.256	1.057	1.144↑	1.240
const	0.920	0.947	0.890	0.851↓	0.936	0.628	0.475	0.221	0.235↑	0.275↑	1.220	1.180	1.112	1.131	1.087
ped	0.262	0.307	0.671	0.732	0.745	6.039	7.537	2.768	2.636	2.516	2.560	2.913	2.157	2.143	1.967
moto	0.866	0.920	0.825	0.830	0.884	1.021	0.573	0.190	0.304↑	0.201	1.572	1.232	1.315	1.293	1.061
bicyc	0.771	0.946	0.949	0.948↓	0.950	1.315	0.649	0.144	0.330↑	0.140	1.764	1.482	1.167	1.177↑	1.064
cone	0.180	0.251	0.572	0.586	0.892	5.189	4.854	1.091	1.123↑	0.898	3.161	2.725	1.550	1.598↑	1.944↑
barrier	0.208	0.410	0.745	0.765	0.896	5.429	4.029	2.128	2.115	1.670	2.303	1.996	1.464	1.490↑	1.041

↓ indicates a performance drop for COUNT, while ↑ means a performance drop for AGG, compared to CN.

Table 13: Result of COUNT and AGGREGATION (nuScenes)

RETRIEVE-SINGLE(10% tolerance)					COUNT				AGG(absolute)				AGG(q-error)			
	CP	CN	CN_{pt}	CN_{pt}^o	CP	CN	$-CN_{pt}$	CN_{pt}^o	CP	CN	CN_{pt}	CN_{pt}^o	CP	CN	CN_{pt}	CN_{pt}^o
car	0.952	0.9156	0.929	0.934	0.692	0.705	0.681	0.701	0.135	0.280	2.25	0.172	1.134	1.159	1.198	1.154
ped	0.602	0.675	0.639	0.792	0.776	0.778	0.781	0.828	0.704	0.167	3.07	0.447	1.724	1.082	1.004	1.0
cyclist	0.760	0.797	0.773	0.812	0.901	0.925	0.922	0.931	0.152	0.121	2.183	0.211	1.0	1.0	1.0	1.0

Table 14: Query result on KITTI dataset

RETRIEVAL-SINGAL(10% tolerance)					COUNT				AGG(absolute)				AGG(q-error)			
	VN	CN	CN_{pt}	CN_{pt}^o	VN	CN	CN_{pt}	CN_{pt}^o	VN	CN	CN_{pt}	CN_{pt}^o	VN	CN	CN_{pt}	CN_{pt}^o
vehicle	0.777	0.817	0.818	0.861	0.828	0.814	0.799	0.835	8.927	6.385	3.595	3.420	1.269	1.242	1.199	1.196
pedestrian	0.776	0.814	0.824	0.852	0.724	0.736	0.738	0.799	8.888	6.501	3.523	3.342	1.271	1.244	1.193	1.197
cyclist	0.784	0.817	0.820	0.852	0.739	0.788	0.776	0.788	8.839	6.289	3.567	3.143	1.265	1.258	1.205	1.199

Table 15: Query result on Waymo dataset

Query Information			ACC					Recall					Precision				
Query	Predict	Selectivity	VN	TF	CN	CN_{pt}	CN_{pt}^o	VN	TF	CN	CN_{pt}	CN_{pt}^o	VN	TF	CN	CN_{pt}	CN_{pt}^o
Q1	RETRIEVAL(car>5)	67.9%	0.812	0.768	0.614	0.778	0.850	0.815	0.769	0.996	0.972	0.929	0.995	0.997	0.615	0.796	0.908
Q2	RETRIEVAL(barrier>3)	76.2%	0.639	0.748	0.859	0.866	0.764	0.954	0.953	0.905	0.893	0.934	0.641	0.752	0.943	0.967	0.807
Q3	RETRIEVAL(bus>0)	33.2%	0.488	0.507	0.553	0.445	0.557	0.504	0.628	0.898	0.762	0.759	0.940	0.949	0.591	0.515	0.632
Q5	RETRIEVAL(car>5, ped>0)	31.5%	0.635	0.604	0.520	0.624	0.702	0.638	0.605	0.967	0.857	0.841	0.962	0.966	0.529	0.697	0.809
Q6	RETRIEVAL(truck>0, barrier>5)	16.8%	0.404	0.448	0.332	0.465	0.529	0.411	0.452	0.761	0.882	0.678	0.964	0.977	0.371	0.496	0.706

Table 16: Case study of different query scenario (nuScenes)

no adjustment		$\epsilon = 0.1$		$\epsilon = 0.15$		$\epsilon = 0.2$	
Model	dist	rate	dist	rate	dist	rate	dist
p2	1116	0.835	339	0.667	168	0.486	90
p2-o0.1	21	0.780	279	0.572	274	0.371	343
p2-o0.2	48	0.811	43	0.624	35	0.433	32
p4	9	0.543	556	0.379	743	0.087	752
p4-o0.1	14	0.650	9	0.379	7	0.178	8
p4-o0.2	4739	0.617	4736	0.337	4734	0.145	4735
p9	20	0.642	0	0.426	3	0.219	3
p9-o0.1	34	0.693	48	0.369	53	0.170	54
p9-o0.2	16	0.684	7	0.439	35	0.231	0

Table 17: Data distribution (abbr. dist) of model selection with adjustment with 9 models (nuScenes)

Model		w/o.Adjust	$\epsilon = 0.1$		$\epsilon = 0.15$		$\epsilon = 0.2$	
pt	o	dist	rate	dist	rate	dist	rate	dist
2	0	0	0.718	0	0.475	0	0.266	0
2	0.1	1171	0.631	641	0.355	561	0.159	713
2	0.2	60	0.633	54	0.358	53	0.161	56
9	0	6	0.616	0	0.336	0	0.144	1
9	0.1	4752	0.405	5323	0.131	5404	0.026	5237
9	0.2	30	0.497	1	0.207	1	0.061	12

Table 18: Data distribution (abbr. dist) of model selection with adjustment with 6 models (nuScenes)

Model		w/o.Adjust	$\epsilon = 0.1$		$\epsilon = 0.15$		$\epsilon = 0.2$	
pt	o	dist	rate	dist	rate	dist	rate	dist
2	0	19	0.833	14	0.663	12	0.481	9
2	0.1	1133	0.809	656	0.621	461	0.429	414
2	0.2	20	0.837	18	0.670	17	0.490	17
4	0	23	0.660	22	0.393	24	0.190	59
4	0.1	22	0.634	17	0.358	13	0.161	14
4	0.2	4728	0.578	4734	0.292	4735	0.112	4734
9	0	26	0.628	19	0.352	18	0.156	19
9	0.1	13	0.593	502	0.309	702	0.124	717
9	0.2	33	0.691	35	0.435	35	0.228	34

Table 19: Data distribution (abbr. dist) of model selection with emphasis on car & pedestrian (nuScenes)

while $CN_{pt=2}^{o=0.1}$ remains the second dominant model. From the results in Figure 14, it is evident that applying adjustments dramatically improves accuracy. When comparing the adjusted results to the best-performing model ($CN_{pt=4}^{o=0.2}$), even the weaker-performing models achieve comparable results through model selection with adjustments.

(2) **Impact of Weight Adjustment on Object Categories.** We also evaluated the effect of adjusting weights for different objects in model selection. Table 19 displays the results when the weights for the “car” and “pedestrian” categories are doubled, compared to the even-weight approach shown in Table 8. From Table 19, the dominant model remains $CN_{pt=4}^{o=0.2}$; however, the second dominant model shifts from $CN_{pt=4}^{o=0}$ to $CN_{pt=9}^{o=0.2}$. As shown in Figure 15, this adjustment significantly improves performance for the “car” and

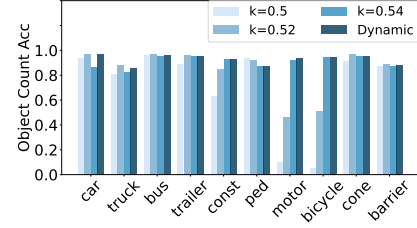


Figure 17: Result of Dynamic Thresholding

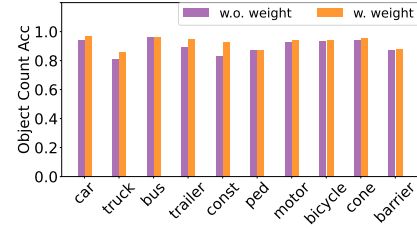


Figure 18: Result of Weighted Loss with Partitioning

“pedestrian” categories, while maintaining stable performance for other object categories.

E.4 Ablation Studies

Dynamic Thresholding. As explained in Section 5.1, we proposed using dynamic thresholding to filter out noise for peak detection. We compared the results with and without dynamic thresholding for the model CN-p4o. In our evaluation, we selected three fixed thresholds: 0.5, 0.52, and 0.54, for comparison. As shown in Figure 17, using a fixed threshold resulted in significant deviations across object categories. For instance, the motorcycle and bicycle categories experienced extremely low performance with thresholds of 0.5 and 0.52, while the car and truck categories, with a threshold of 0.54 performed poorly. In contrast, dynamic thresholding provided a more balanced performance across all categories, achieving consistently good results.

Weighted loss. In Section 5.1, we introduced the weighted loss during the model training with partitions. We introduce the weighted loss intent to improve the prediction with the frame with more objects appear. By refer to the data statistics of nuScenes dataset in Appendix E.1, we can see that the weighted loss contributed more to the low frequency objects, such as truck, trailer and construction vehicles. While for the high frequency appearance objects, such as car, pedestrian, and barrier, the improvement with partition is limited.

F Additional Experiment on KITTI

We evaluate our proposed method on the KITTI dataset. We use CenterPoint(CP) [49] as the baseline detection model.

Model		w/o.Adjust	$\epsilon = 0.05$		$\epsilon = 0.1$		$\epsilon = 0.15$	
pt	o	dist	rate	dist	rate	dist	rate	dist
2	0	937	0.956	0	0.838	0	0.672	0
2	0.2	597	0.555	94	0.095	1052	0.005	1648
4	0	512	0.775	0	0.362	0	0.101	61
4	0.2	165	0.307	3675	0.008	2717	0.00002	2060
9	0	1525	0.965	0	0.868	0	0.728	0
9	0.2	33	0.890	0	0.628	0	0.351	0

Table 20: Data distribution (abbr. dist) of model selection with adjustment (KITTI)

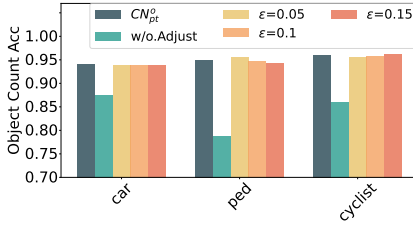


Figure 19: Model selection (KITTI)

F.1 Categorical Query Results

As shown in Table 14 and Table 4, the performance improvement of our proposed CounterNet (CN) on the KITTI dataset is less pronounced compared to the improvements observed on the nuScenes dataset when compared to the detection model CenterPoint (CP). For the SELECT-COUNT operation, while the performance improvements for the "car" and "cyclist" categories are not substantial, a noticeable improvement is observed for the "pedestrian" category.

Regarding partitioning and overlap, the results for our proposed solution are consistent with those observed on the nuScenes dataset. However, considering that the scene scale of nuScenes is approximately four times larger than that of KITTI, partitioning has a more negative impact on performance in the KITTI dataset. Nevertheless, the use of overlap partially mitigates this negative effect.

F.1.1 Model Selection. Table 20 and Figure 19 present the results of model selection with six models on the KITTI dataset. Overall, the findings are consistent with those observed on the nuScenes dataset. As shown in Table 20, after applying the adjustment, the frames are primarily concentrated on four partitions with a 0.2 overlap rate ($CN_{pt=4}^{o=0.2}$) and two partitions with a 0.2 overlap rate ($CN_{pt=2}^{o=0.2}$). Furthermore, as illustrated in Figure 19, similar to the nuScenes results, the model selection yields balanced performance across all categories.

G Results on Waymo dataset

We use a subset of the dataset for evaluation, consisting of 18,583 training point clouds and 4,932 for evaluation. The data is sourced from segments prefixed with segment-1 and segment-2. Table 15 presents the categorical query results on the Waymo dataset. Overall, the results exhibit similar trends to those observed on the other datasets.

H Case studies

We evaluate the performance of the actual query across different scenarios and levels of selectivity on the nuScenes dataset. The experimental results assess accuracy, precision, and recall. The key observations are as follows: (1) Accuracy. Our proposed method consistently outperforms the baseline methods in terms of accuracy. However, when precision and recall are considered, the performance varies depending on the specific query. (2) Selectivity. Overall, performance is better in high-selectivity scenarios, whereas low-selectivity cases introduce more errors across all methods. (3) Query-Specific Analysis. For Query 1 (Q1), CounterNet exhibits a tendency toward higher recall compared to precision, whereas the baselines demonstrate the opposite trend. This indicates that CounterNet achieves higher accuracy within the queried frames but may fail to select some relevant frames. In contrast, the baseline methods tend to select a larger number of frames, capturing more true-positive frames. However, their lower precision indicates reduced accuracy among the selected frames. A similar trend is observed across all other queries.

Received 20 February 2007; revised 12 March 2009; accepted 5 June 2009